Thermo X https://doi.org/10.70401/tx.2026.0036

Supplementary information

Transient thermal response and regulation of transparent silica aerogels under fluctuating solar irradiance

Shiteng Li, Ningxin Yang, Fujie Li, Shang Liu, Chun Li, Shuai Deng, Meng Lin

Thermo X https://doi.org/10.70401/tx.2026.0036

Supplementary information

Transient thermal response and regulation of transparent silica aerogels under fluctuating solar irradiance

Shiteng Li, Ningxin Yang, Fujie Li, Shang Liu, Chun Li, Shuai Deng, Meng Lin

Contents

Supporting Note S1. Materials, sample preparation, and experimental methods **..4**

S1.1 Materials 4

S1.2 Synthesis of transparent silica aerogels 4

S1.3 Preparation of the solar absorber 5

S1.4 Optical and thermal characterization 5

S1.5 Stagnation temperature experiment 6

S1.6 Experimental uncertainty analysis 7

Supporting Note S2. Unified physical and mathematical model **..... 9**

S2.1 Physical processes and modeling assumptions 9

S2.2 Computational domains and operating configurations 9

S2.3 Governing equations 11

S2.4 Initial and boundary conditions 14

S2.5 Thermophysical and optical properties 15

Supporting Note S3. Spectral radiation treatment **..... 17**

S3.1 Mie-Theory calculation of the infrared absorption coefficient 17

S3.2 5-band approximation of the infrared absorption spectrum 17

S3.3 Spectral band independence analysis 18

Supporting Note S4. Numerical solution and model verification **..... 20**

S4.1 Numerical implementation 20

S4.2 Mesh independence analysis 20

S4.3 Relative tolerance independence analysis 21

S4.4 Angular quadrature independence analysis 21

S4.5 Finite size effects and calibration of the 2D reduced order model 22

S4.6 Sensitivity to short-wave solar absorption in the aerogel 26

Supporting Note S5. Heat flux evaluation **..... 28**

Supporting Note S6. Step response analysis **..... 29**

S6.1 Step response protocol 29

S6.2 Response time extraction and curve fitting 29
S6.3 Complete response metrics 29

Supporting Note S7. Implementation of GHI-driven flow regulation **31**

S7.1 The GHI measurements in Shenzhen 31
S7.2 Solar receiver system configuration 32
S7.3 Operating map construction and interpolation 32
S7.4 Inlet velocity schedules 33
S7.5 Implementation workflow of GHI-driven flow regulation 34

References **36**

Supporting Note S1. Materials, sample preparation, and experimental methods

S1.1 Materials

Tetramethyl orthosilicate (TMOS, 98.0%), ammonia solution in methanol (2.0 M), methanol (analytical reagent grade, 99.5%), chlorotrimethylsilane (CTMS, gas chromatography grade, >98.0%), ethanol (analytical reagent grade, 95.0%), and nanocarbon powder were purchased from Aladdin Biochemical Technology Co., Ltd. A copper sheet with dimensions of 30 mm × 30 mm × 0.3 mm was purchased from Dongguan Guanfeng Metal Materials Co., Ltd. and used as the substrate for the solar absorber. Deionized water was prepared in the laboratory. All chemicals and materials were used as received without further purification unless otherwise specified.

S1.2 Synthesis of transparent silica aerogels

Transparent silica aerogels were synthesized through a one-step sol-gel process followed by hydrophobic modification, supercritical drying, and thermal annealing[1,2]. TMOS was used as the silica precursor, a 2.0 M ammonia solution in methanol was used as the base catalyst, methanol was used as the solvent, and deionized water was used for hydrolysis. TMOS and the ammonia-methanol solution were separately diluted with methanol before mixing. Deionized water was subsequently added, and the precursor solution was stirred until a homogeneous sol was obtained. The molar ratio of NH_3:TMOS:water:CH_3OH = 0.006:1:3:7.

The resulting sol was poured into preassembled molds and allowed to gel under ambient conditions. After gelation, the wet gels were immersed in ethanol for solvent exchange. The ethanol was replaced 5 times to remove residual water, methanol, unreacted precursors, and reaction by-products. The solvent-exchanged gels were then immersed in a CTMS-ethanol solution with a CTMS-to-ethanol volume ratio of 1:9 for 24 h to render the silica network hydrophobic. After surface modification, the gels were washed with ethanol for an additional 3 cycles to remove residual CTMS and associated reaction products. The hydrophobically modified wet gels were transferred to a supercritical drying vessel. The temperature and pressure were increased to minimize

thermal and mechanical stresses within the gel network. Solvent extraction was maintained under supercritical conditions for 10 h. After drying, the pressure was reduced from 9.5 MPa to ambient pressure at a controlled exhaust flow rate of 50 mL min^{-1}, thereby minimizing structural shrinkage and cracking during depressurization. The dried aerogels were annealed at 200 ^{o}C for 24 h to improve their optical transmittance. The resulting transparent silica aerogels were monolithic and had dimensions of 30 mm × 30 mm × 12.6 mm.

S1.3 Preparation of the solar absorber

The solar absorber was prepared by depositing a nanocarbon powder coating onto a copper substrate. A copper sheet with dimensions of 30 mm × 30 mm × 0.3 mm was first cleaned with ethanol to remove surface contaminants and dried at 50 ^{o}C. Nanocarbon powder was uniformly dispersed in ethanol to form a stable suspension. A Nafion solution was added as a binder to improve the adhesion of the nanocarbon particles to the copper surface. The suspension was mixed until homogeneous and then spray-coated onto one side of the precleaned copper sheet using a spray gun. During coating, the copper substrate was maintained at 60 ^{o}C to facilitate solvent evaporation and promote the formation of a uniform absorbing layer.

S1.4 Optical and thermal characterization

The wavelength-dependent optical properties of the transparent silica aerogel and solar absorber were measured using a UV-Visible-Near infrared spectrophotometer equipped with an integrating sphere (LAMBDA 750S, PerkinElmer). The measurements were performed over the wavelength range of 250–2500 nm with an incident beam size of 5 mm × 10 mm. The integrating sphere was used to collect both directly transmitted and diffusely scattered radiation. The total spectral transmittance (τ_λ) of the silica aerogel was measured directly. For the solar absorber, the total spectral reflectance (R_λ) was measured. Because the copper substrate was opaque over the investigated wavelength range, its spectral transmittance was assumed to be 0. The spectral absorptance of the absorber was therefore calculated as

$$\alpha_\lambda = 1 - R_\lambda \tag{S1}$$

The solar-weighted total transmittance of the silica aerogel was calculated by weighting the measured spectral transmittance with the AM 1.5G solar spectral irradiance

$$\overline{\tau}_{\text{solar}} = \frac{\int_{\lambda_1}^{\lambda_2} \tau_\lambda I_{\text{AM1.5G},\lambda}\, \mathrm{d}\lambda}{\int_{\lambda_1}^{\lambda_2} I_{\text{AM1.5G},\lambda}\, \mathrm{d}\lambda} \tag{S2}$$

where $I_{\text{AM1.5G},\lambda}$ is the wavelength-dependent AM 1.5G solar spectral irradiance. Similarly, the solar-weighted absorptance of the absorber was calculated as

$$\overline{\alpha}_{\text{solar}} = \frac{\int_{\lambda_1}^{\lambda_2} \alpha_\lambda I_{\text{AM1.5G},\lambda}\, \mathrm{d}\lambda}{\int_{\lambda_1}^{\lambda_2} I_{\text{AM1.5G},\lambda}\, \mathrm{d}\lambda} \tag{S3}$$

The effective thermal conductivity of the silica aerogel was measured using a custom-built steady-state heat flow meter apparatus. The aerogel sample was placed between temperature-controlled hot and cold plates maintained at 33 ^{o}C and 13 ^{o}C, respectively. The measured effective thermal conductivity of the transparent silica aerogel was 0.015 W m^{-1} K^{-1} at a mean temperature of 23 ^{o}C. After steady state was reached, the effective thermal conductivity was determined from the measured heat flux and temperature difference according to Fourier's law.

S1.5 Stagnation temperature experiment

The transient stagnation temperature response of the aerogel covered absorber was measured using the experimental setup shown in Fig. S1. The setup consisted of a solar simulator, an aluminum aperture, silica aerogel, solar absorber, thermocouples, and a data acquisition system. Before each experiment, the irradiance at the absorber plane was calibrated to 1000 W m^{-2} using a photoradiometer (PL-MW2000, Beijing Perfectlight Technology Co., Ltd., China). The absorber was covered directly by a transparent silica aerogel. The bottom and lateral surfaces of the absorber were insulated using insulation materials to minimize parasitic heat losses. An aluminum

aperture was positioned above the insulation to reflect incident radiation away from the area outside the absorber, thereby restricting the illuminated area to the active absorber surface. 3 K-type thermocouples (Kepsen Measurement and Control Technology Co., Ltd., Taizhou, China) were used to monitor the absorber surface temperature, the upper surface temperature of the silica aerogel, and the ambient temperature. The thermocouple signals were recorded using an 8-channel thermocouple data acquisition module (TC-08, OMEGA Engineering, Inc.). The absorber thermocouple was positioned at the center of the absorber surface beneath the aerogel, while the aerogel surface thermocouple was positioned at the center of the exposed upper surface. Temperature recording was initiated simultaneously with activation of the solar simulator and continued for 7200 s under constant 1000 W m^{-2}.

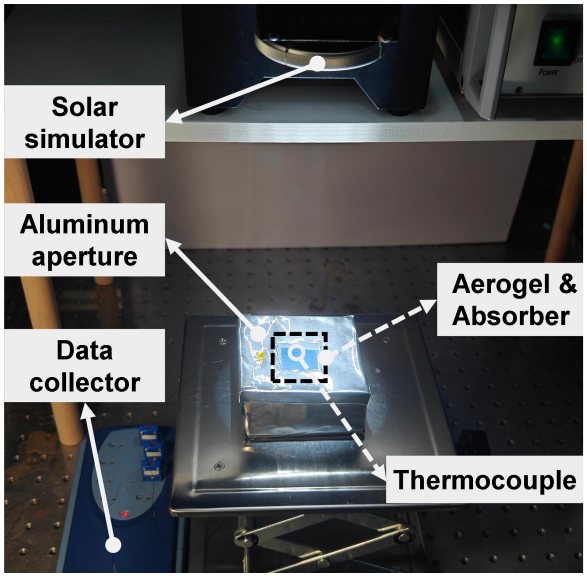


Figure S1. Experimental setup for stagnation temperature measurements.

S1.6 Experimental uncertainty analysis

The experimental uncertainty was evaluated based on the accuracy specifications of the measurement instruments used in this study. The uncertainties associated with the incident solar irradiance, temperature measurement, optical property characterization, and thermal conductivity measurement were quantified individually. Where multiple independent uncertainty sources contributed to the same measured quantity, they were combined using the root-sum-square method.

The uncertainty of the incident solar irradiance was determined from the specification of the photoradiometer used for solar simulator calibration, with a measurement accuracy of ±2.5%.

The temperature uncertainty was obtained by combining the uncertainty of the K-type thermocouple and TC-08 data acquisition system:

$$u_T = \sqrt{u_{TC}^2 + u_{DAQ}^2} \tag{S4}$$

where u_{TC} and u_{DAQ} are ±1.5 ºC and ±0.5 ºC, respectively. The resulting temperature measurement uncertainty was ±1.6 ºC. The optical property uncertainty was estimated from the photometric accuracy of the LAMBDA 750S spectrophotometer (±0.003 A). The corresponding uncertainty of spectral transmittance and reflectance measurements was approximately ±0.6%. The uncertainty of thermal conductivity measurement was taken as ±3% according to the specification of the heat flow measurement system. The uncertainty values of all experimental measurements are summarized in Table S1.

Table S1. Summary of experimental measurement uncertainties.

Parameter	Measurement method	Uncertainty
Solar irradiance	Photoradiometer	±2.5%
Temperature	K-type thermocouple combined with TC-08 data logger	±1.6 °C
Spectral transmittance	LAMBDA 750S spectrophotometer	±0.6%
Spectral reflectance	LAMBDA 750S spectrophotometer	±0.6%
Thermal conductivity	Heat flow measurement system	±3%

Supporting Note S2. Unified physical and mathematical model

S2.1 Physical processes and modeling assumptions

A unified two-dimensional (2D) transient modeling framework was developed for the aerogel covered solar absorber, with the active computational domains selected according to the stagnation or fluid flow configuration. The complete model included the silica aerogel, solar absorber, insulation material, and fluid channel. It accounted for transient heat storage, solid conduction, non-gray thermal radiation transport within the aerogel, conjugate heat transfer to the working fluid, laminar flow, and heat loss to the surroundings[6,7]. Short-wave solar input was applied to the absorber using the measured aerogel transmittance and absorber absorptance, while long-wave thermal radiation was resolved within the aerogel[8].

The stagnation temperature configuration was obtained by removing the fluid domain and useful heat extraction. The conduction only and radiation only cases were derived from the stagnation temperature model by deactivating internal radiation or setting the aerogel thermal conductivity to 0, respectively. External convective and radiative heat losses were retained in all cases.

The main assumptions were: *(i)* the aerogel was treated as a homogeneous and isotropic effective continuum; *(ii)* local thermal equilibrium was assumed between the silica skeleton and pore gas; *(iii)* effective thermophysical properties were spatially uniform and temperature independent; *(iv)* direct absorption of short-wave solar radiation within the silica aerogel was neglected in the baseline model because an additional sensitivity analysis showed only a minor influence on the predicted absorber and upper aerogel surface temperatures (Section S4.6); *(v)* the liquid was single-phase, incompressible, Newtonian, and laminar; *(vi)* gravity and buoyancy were neglected; *(vii)* interfacial thermal resistance was neglected.

S2.2 Computational domains and operating configurations

S2.2.1 Stagnation temperature configuration

The stagnation temperature model comprised a 30 mm-long solar absorber covered by a silica aerogel of the same lateral dimension. The aerogel and absorber thicknesses were 12.6 mm and 0.3 mm, respectively. Both components were embedded in an insulation domain with an overall width of 70 mm and height of 40 mm, as shown in Fig. S2.

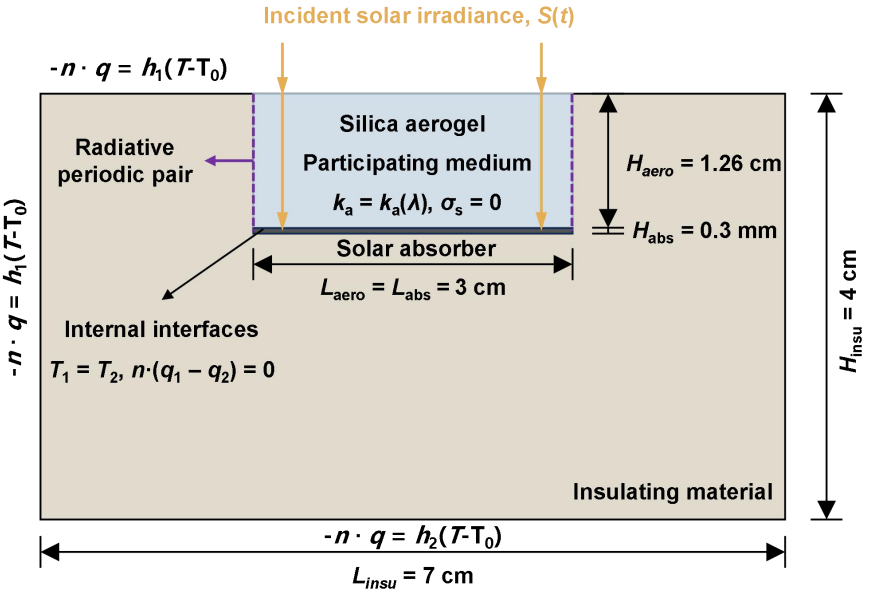


Figure S2. Computational domain of the stagnation temperature configuration.

Incident solar irradiance was applied over the illuminated region, and the transmitted solar energy was absorbed by the absorber. Heat was transferred through the aerogel by coupled conduction and non-gray thermal radiation and was rejected to the surroundings through the exposed surface and the external insulation boundaries. Temperature and heat flux were continuous across all internal interfaces. The periodic condition was applied only to the radiative intensity field at the lateral boundaries of the participating aerogel domain.

S2.2.2 Fluid flow configuration

The fluid flow configuration consisted of a 100 mm-long silica aerogel layer, solar absorber, and fluid channel, as shown in Fig. S3. The aerogel thickness was 12.6 mm, the absorber thickness was 0.3 mm, and the channel height was 2 mm. The fluid channel

was located beneath the absorber, allowing heat to be transferred from the absorber to the flowing liquid through conjugate heat transfer.

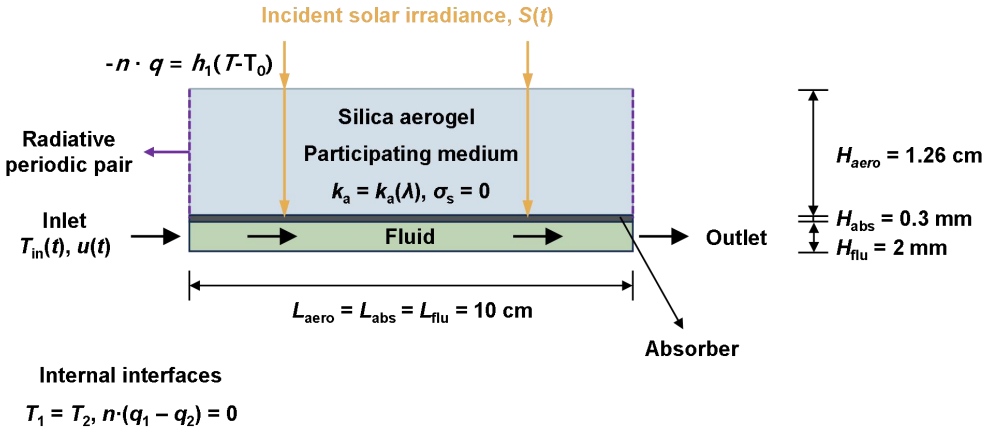


Figure S3. Computational domain of the fluid flow configuration.

The liquid entered the channel at 22 °C with a prescribed inlet velocity and exited through a pressure outlet boundary. No-slip conditions were imposed on the channel walls. The inlet velocity was held constant in the step response simulations and was varied with time in the solar irradiance driven regulation simulations.

S2.3 Governing equations

S2.3.1 Energy conservation in the solid domains

Transient energy conservation in the absorber and insulation is

$$\rho_i c_{p,i} \frac{\partial T_i}{\partial t} = \nabla \cdot \left(k_i \nabla T_i \right) \tag{S5}$$

where i is the absorber or insulation domain, ρ_i is the density, $c_{p,i}$ is the specific heat capacity, k_i is the thermal conductivity, and T_i is the local temperature. No volumetric heat generation was included in these domains. The absorbed solar energy was imposed separately as a boundary heat source at the illuminated absorber surface, as described in Section S2.4.1.

In the aerogel, heat conduction is coupled with radiative energy transport through

$$\rho_{\text{aero}}\, c_{p,\,\text{aero}} \frac{\partial T}{\partial t} = \nabla \cdot \left(k_{\text{aero}} \nabla T \right) - \nabla \cdot \mathbf{q}_{\text{rad}} \tag{S6}$$

where ρ_{aero}, $c_{p,\text{aero}}$, and k_{aero} are the density, specific heat capacity, and thermal conductivity of the aerogel, respectively, and $\mathbf{q}_{\text{rad}}$ is the total radiative heat flux defined in Eq. (S10). The term $-\nabla\cdot\mathbf{q}_{\text{rad}}$ is the net volumetric radiative energy source within the aerogel. It couples the radiative transport field to the temperature field, while the temperature dependent emission term in the radiative transfer equation provides the reciprocal coupling.

S2.3.2 Non-gray radiative transfer in the aerogel

For spectral band *b*, the general radiative transfer equation for an absorbing, emitting, and scattering participating medium can be written as

$$\mathbf{s}\cdot\nabla I_b(\mathbf{x},\mathbf{s},t)=\overline{k}_b I_{b,\text{bb}}(T)-\overline{\beta}_b I_b(\mathbf{x},\mathbf{s},t)+\frac{\overline{\sigma}_{s,b}}{4\pi}\int_{4\pi} I_b\left(\mathbf{x},\mathbf{s}',t\right)\Phi_b\left(\mathbf{s}',\mathbf{s}\right)\mathrm{d}\Omega' \qquad \text{(S7)}$$

where $I_{\text{b}}(\boldsymbol{x}, \mathbf{s}, t)$ is the band integrated radiative intensity at position $\boldsymbol{x}$ in direction $\mathbf{s}$, $I_{\text{b,bb}}(T)$ is blackbody radiative intensity integrated over spectral band *b*, $\overline{k}_b$ is the band-averaged absorption coefficient, $\overline{\sigma}_{s,b}$ is the band averaged scattering coefficient, $\overline{\beta}_b=\overline{k}_b+\overline{\sigma}_{s,b}$ is the extinction coefficient. $\Phi_b\left(\mathbf{s}',\mathbf{s}\right)$ is the scattering phase function from incident direction $\mathbf{s}'$ to propagation direction s, and Ω is the solid angle.

For the silica aerogel considered here, long wave scattering was neglected because its contribution was negligible compared with absorption over the investigated thermal infrared range. Therefore

$$\overline{\sigma}_{s,b}=0,\quad \overline{\beta}_b=\overline{k}_b \qquad \text{(S8)}$$

and the scattering source term vanishes. The radiative transfer equation used in the present model consequently reduces to

$$\mathbf{s}\cdot\nabla I_b(\mathbf{x},\mathbf{s},t)=\overline{k}_b\left[I_{b,\text{bb}}(T)-I_b(\mathbf{x},\mathbf{s},t)\right] \qquad \text{(S9)}$$

The corresponding total radiative heat flux is obtained by integrating the directional

intensity over all solid angles and summing over the spectral bands

$$\mathbf{q}_{\text{rad}} = \sum_{b=1}^{N_b} \int_{4\pi} I_{\text{b}}\left(\mathbf{x}, \mathbf{s}, t\right) \mathbf{s} \mathrm{d}\Omega \tag{S10}$$

where N_{b} is the number of spectral bands. The angular dependence of Eq. (S9) was discretized using the discrete ordinates method, as described in Section S4.1.

S2.3.3 Fluid flow equations

For incompressible flow

$$\nabla \cdot \mathbf{u} = 0 \tag{S11}$$

$$\rho_f \left[\frac{\partial \mathbf{u}}{\partial t} + (\mathbf{u} \cdot \nabla)\mathbf{u} \right] = \nabla \cdot \left[-p\mathbf{I} + \sigma_v \right] \tag{S12}$$

where $\sigma_v = \mu_f \left[\nabla \mathbf{u} + (\nabla \mathbf{u})^{\text{T}} \right]$ is the viscous stress tensor. The **u** is the fluid velocity vector, p is the pressure, ρ_f is the fluid density, μ_f is the dynamic viscosity, and **I** is the identity tensor. No body force was included in the momentum equation.

The fluid energy equation is

$$\rho_f c_{p,f} \left(\frac{\partial T}{\partial t} + \mathbf{u} \cdot \nabla T \right) = \nabla \cdot \left(k_f \nabla T \right) \tag{S13}$$

where T is the fluid temperature, $c_{p,f}$ is the specific heat capacity, and k_f is the thermal conductivity of the fluid. Viscous dissipation and pressure work were neglected.

S2.3.4 Interfacial continuity

At interfaces without an imposed boundary heat source, temperature and normal heat flux were continuous

$$T_1 = T_2 \tag{S14}$$

$$\mathbf{n} \cdot \left(\mathbf{q}_1 - \mathbf{q}_2 \right) = 0 \tag{S15}$$

q is the total normal heat flux, including radiative flux where applicable. No contact resistance was included.

S2.4 Initial and boundary conditions

S2.4.1 Solar input

The absorbed solar heat flux was imposed as a boundary heat source on the illuminated absorber surface according to Eq. (1) of the main text. The stagnation temperature validation was performed at G = 1000 W m^{-2}. The coupling simulations used 1000 W m^{-2} for 0–7200 s followed by 600 W m^{-2} for 7200–14400 s. The fluid step response simulations used 1000 W m^{-2} for 0–3600 s followed by 600 W m^{-2} for 3600–7200 s. The global horizontal irradiance (*GHI*) driven calculations used measured Shenzhen profiles.

S2.4.2 External heat exchange

Convective heat exchange with the surroundings was imposed using a convective heat flux boundary condition

$$-\mathbf{n}\cdot\mathbf{q}_{\text{cond}} = h\left(T - T_{\infty}\right) \tag{S16}$$

where $\mathbf{n}$ is the outward unit normal vector, $\mathbf{q}_{\text{cond}} = -k\nabla T$ is the conductive heat flux, h is the convective heat transfer coefficient, In the stagnation configuration, h_1 = 10 W m^{-2} K^{-1} was applied to the exposed upper and lateral boundaries, while h_2 = 8 W m^{-2} K^{-1} was applied to the lower insulation boundary.

For the fully coupled and radiation only cases, long wave radiative exchange at the exposed aerogel surface was treated directly through the band resolved semitransparent surface condition of the participating medium radiation model. The external radiative field was prescribed at T_{∞} = 22 °C, and radiative emission, reflection, and transmission were evaluated separately for each spectral band. Therefore, no additional gray surface radiation boundary condition was imposed at this surface when participating medium radiation was active. The model explicitly applied the semitransparent surface treatment to the aerogel boundary and used the ambient temperature for the external radiation field.

In the conduction only diagnostic case, participating medium radiation was deactivated while external radiative heat loss was retained using a surface to ambient radiation boundary condition

$$q_{\text{loss, rad}}'' = \varepsilon\sigma\left(T^4 - T_\infty^4\right) \tag{S17}$$

where ε is the surface emissivity and σ is the Stefan-Boltzmann constant. An emissivity of ε = 0.98, and an ambient radiation temperature of 22 °C were used for this boundary.

S2.4.3 Fluid inlet and outlet

At the inlet,

$$\mathbf{u} = v_{\text{in}}(t)\mathbf{e}_x, \quad T = T_{\text{in}} = 22^{\text{o}}\text{C} \tag{S18}$$

A pressure outlet and convective energy outflow were applied at the channel exit. No-slip conditions were applied at channel walls. The initial temperature of all domains was 22 °C unless otherwise specified.

S2.5 Thermophysical and optical properties

The thermophysical and optical properties used in the numerical model are summarized in Table S2. The measured thermal conductivity and solar transmittance of the silica aerogel, together with the measured solar absorptance of the absorber, were used directly in the simulations. The remaining thermophysical properties were treated as constant over the investigated temperature range. Long-wave radiative properties of the aerogel were represented separately using the spectral model described in Supporting Note S3.

Table S2. Thermophysical and optical properties used in the model.

Material	Parameter	Value
Aerogel	Thermal conductivity	0.015 W m^{-1} K^{-1}
	Density	200 kg m^{-3}
	Specific heat capacity	670 J kg^{-1} K^{-1}
	Transmittance	90%
	Scattering coefficient	0 m^{-1}
Absorber	Thermal conductivity	380 W m^{-1} K^{-1}
	Density	8930 kg m^{-3}
	Specific heat capacity	420 J kg^{-1} K^{-1}
	Solar absorptance	98%
Insulation material (calibrated 2D model)	Thermal conductivity	0.026 W m^{-1} K^{-1}
	Density	180 kg m^{-3}
	Specific heat capacity	670 J kg^{-1} K^{-1}
Fluid (silicone oil)	Thermal conductivity	0.12 W m^{-1} K^{-1}
	Density	1002 kg m^{-3}
	Specific heat capacity	1560 J kg^{-1} K^{-1}
	Dynamic viscosity	0.1 Pa s

Supporting Note S3. Spectral radiation treatment

S3.1 Mie-Theory calculation of the infrared absorption coefficient

The wavelength-dependent absorption coefficient (k_λ) of the silica aerogel was calculated over the thermal infrared range of 2.5–20 μm using Lorenz-Mie theory. The aerogel skeleton was represented by equivalent spherical silica particles dispersed in air. The particle size and wavelength-dependent complex refractive index[2] were used as inputs to the open-source BHMIE code[9]. Because water contributes to infrared absorption, a water mass fraction of 8% in the silica aerogel was included in the optical property calculation[2,10]. The contribution of water was incorporated into the effective complex refractive index used in the Mie calculation.

For each wavelength, the code calculated the extinction ($Q_{\text{ext},\lambda}$) and scattering ($Q_{\text{sca},\lambda}$) efficiencies. The absorption efficiency ($Q_{\text{abs},\lambda}$) was obtained as

$$Q_{\text{abs},\lambda} = Q_{\text{ext},\lambda} - Q_{\text{sca},\lambda} \tag{S19}$$

For a spherical particle with radius r, the corresponding absorption cross-section was calculated as

$$C_{\text{abs},\lambda}(r) = \pi r^2 Q_{\text{abs},\lambda}(r) \tag{S20}$$

The k_λ of the aerogel was then determined by integrating the absorption cross-section over the particle number distribution

$$k_\lambda = N_p C_{\text{abs},\lambda} \tag{S21}$$

where N_p is the particle number density. The calculated long-wave scattering contribution was negligible compared with absorption over the investigated wavelength range. The aerogel was therefore treated as a non-scattering, absorbing emitting participating medium in the heat transfer model, with

$$\sigma_{\text{s},\lambda} = 0 \tag{S22}$$

S3.2 5-band approximation of the infrared absorption spectrum

The continuous absorption spectrum was reduced to a finite number of spectral bands to retain the principal transparent windows and strong absorption regions while limiting the computational cost of the transient radiation calculation. For band *b*, bounded by $\lambda_{b,1}$ and $\lambda_{b,2}$, the band-averaged absorption coefficient, $\overline{k}_b$, was calculated using a Planck-weighted average

$$\overline{k}_b\left(T_{\mathrm{ref}}\right)=\frac{\int_{\lambda_{b,1}}^{\lambda_{b,2}} k_\lambda E_\lambda^{\mathrm{bb}}\left(T_{\mathrm{ref}}\right)\mathrm{d}\lambda}{\int_{\lambda_{b1}}^{\lambda_{b,2}} E_\lambda^{\mathrm{bb}}\left(T_{\mathrm{ref}}\right)\mathrm{d}\lambda} \tag{S23}$$

where E_λ^{bb} is the spectral blackbody emissive power, and T_{ref} is the representative temperature used for spectral averaging. A reference temperature of 200 °C was selected to represent the characteristic absorber temperature.

The band boundaries were selected according to the major changes in the calculated infrared absorption spectrum. Boundaries at 5.2, 7.0, 9.0, and 13.0 μm separate the principal weakly and strongly absorbing regions. The resulting 5-band properties are summarized in Table S3.

Table S3. Spectral properties used in the 5-band radiation model.

Band	Wavelength interval (μm)	$\overline{k}_b$ (m^{-1})
1	2.5–5.2	991.1
2	5.2–7.0	1441.4
3	7.0–9.0	107608.1
4	9.0–13.0	9370.9
5	13.0–20.0	5726.4

S3.3 Spectral band independence analysis

Spectral band independence was evaluated using 1, 3, 5, and 7 spectral bands. As shown in Fig. S4, taking the 7-band model as the reference, the maximum deviations in absorber temperature were 17.31, 6.37, and 1.27 °C for the 1-band, 3-band, and 5-band models, respectively. The corresponding maximum deviations in the upper aerogel

surface temperature were 3.24, 2.01, and 0.20 °C. Further increasing the spectral resolution from 5-band to the 7-band model, therefore produced only minor changes in the predicted transient temperatures. Considering both numerical accuracy and computational cost, the 5-band model was adopted for the subsequent calculations.

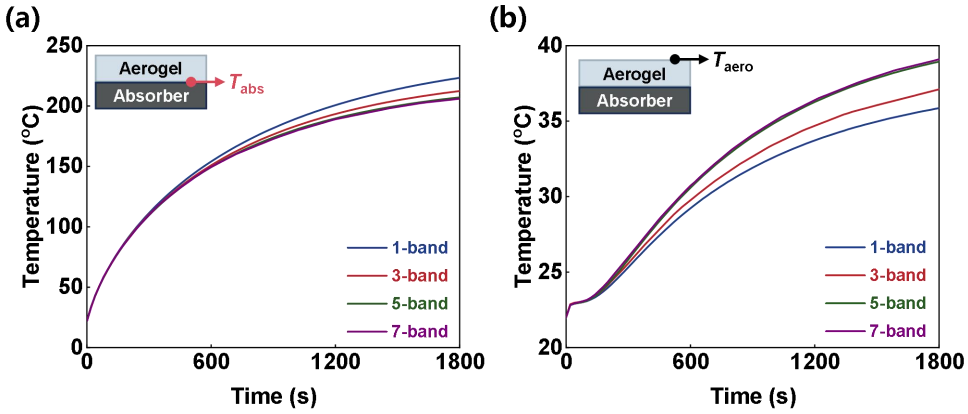


Figure S4. Spectral band independence of the transient temperatures of the absorber and upper aerogel surface.

Supporting Note S4. Numerical solution and model verification

S4.1 Numerical implementation

The governing equations were solved using COMSOL Multiphysics 6.1 with a 2D finite element method[11]. Heat conduction and participating medium radiation were coupled through the *Heat Transfer with Radiation in Participating Media* formulation, while laminar flow and fluid energy transport were solved for the fluid flow configuration. The band-resolved radiative transfer equation was angularly discretized using the discrete ordinates method.

The time-dependent calculations were performed for stagnation heating, irradiance step responses, and *GHI*-driven flow regulation. The transient calculations employed an adaptive backward differentiation formula scheme with a maximum order of 2. For the *GHI*-driven simulations, the maximum internal time step was restricted to 1 s to adequately resolve the 5-s transition between successive inlet velocity setpoints.

The mesh, solver relative tolerance, and angular quadrature were varied independently, while all other numerical settings were held fixed. Their final values were selected based on Sections S4.2–S4.4.

S4.2 Mesh independence analysis

Mesh independence was evaluated using 6 meshes with N_{mesh} = 1165, 1642, 2195, 2826, 3223, and 4446 elements. As shown in Fig. S5, the predicted temperature histories became less sensitive to mesh refinement. Taking N_{mesh} = 4446 as the reference, the maximum deviations obtained with N_{mesh} = 2826 over the entire transient period were 0.57 °C for the absorber temperature and 0.09 °C for the upper aerogel surface temperature. Further mesh refinement produced only minor changes in the temperature histories. Considering both numerical accuracy and computational cost, N_{mesh} = 2826 was adopted for the subsequent calculations.

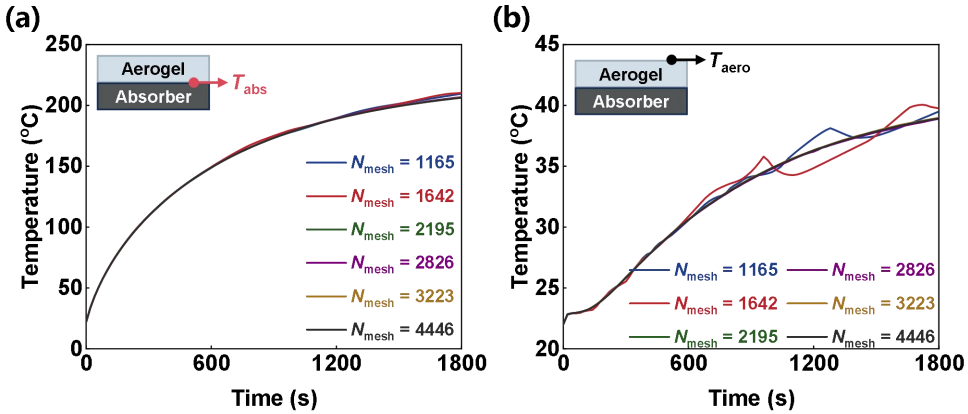


Figure S5. Mesh independence of the transient temperatures of the absorber and upper aerogel surface.

S4.3 Relative tolerance independence analysis

The sensitivity of the transient solution to the relative tolerance was examined using values of 10^{-2}, 10^{-3}, 10^{-4}, and 10^{-5}. As shown in Fig. S6, taking the 10^{-5} solution as the reference, the maximum deviations in absorber and upper aerogel surface temperatures were 8.48 and 1.37 °C at 10^{-2}, respectively, but decreased to 0.11 and 0.08 °C at 10^{-3}. Further reducing the tolerance to 10^{-4} decreased the corresponding deviations to only 0.02 and 0.01 °C. The results obtained with 10^{-3} were therefore considered sufficiently converged, and this value was used in the subsequent calculations.

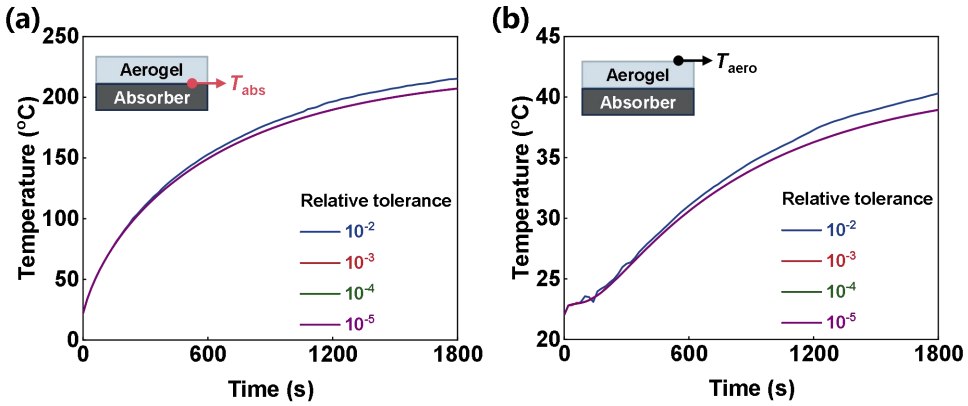


Figure S6. Effect of relative tolerance on the transient temperatures of the absorber and upper aerogel surface.

S4.4 Angular quadrature independence analysis

Angular quadrature independence was evaluated using the S_2, S_4, S_6, and S_8 discrete ordinates schemes. As shown in Fig. S7, taking S_8 as the reference, the maximum deviations in absorber and upper aerogel surface temperatures were 0.57 and 3.19 °C for S_2, respectively, and decreased to 0.16 and 0.68 °C for S_4. Further increasing the angular order to S_6 reduced the corresponding deviations to 0.06 and 0.22 °C. Considering both numerical accuracy and computational cost, the S_4 scheme was adopted for the subsequent calculations.

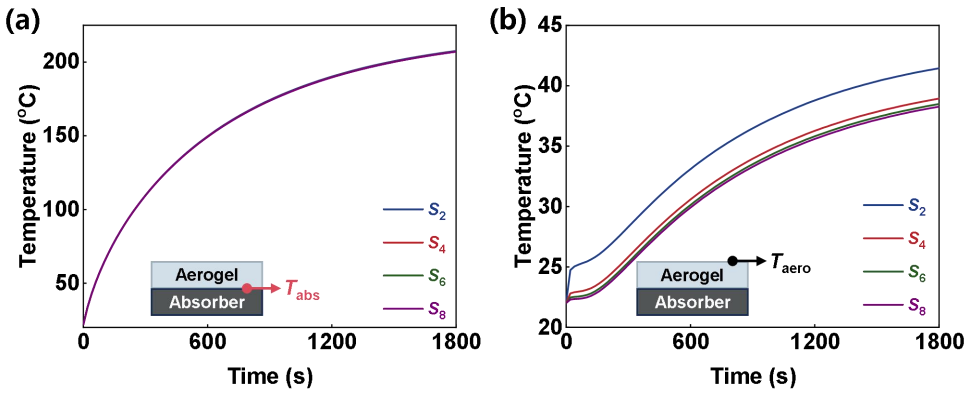


Figure S7. Angular quadrature independence of the transient temperatures of the absorber and upper aerogel surface using the S_2, S_4, S_6, and S_8 discrete ordinates schemes.

S4.5 Finite size effects and calibration of the 2D reduced order model

Because the experimental receiver has finite lateral dimensions, an additional full 3D model was constructed to quantify the associated finite size effects. The 3D model reproduced the actual experimental geometry and used the independently determined thermophysical and optical properties, including the intrinsic thermal conductivity of the insulation material. The incident irradiation, initial condition, and external heat transfer boundary conditions were identical to those used for the stagnation experiment. Temperatures were evaluated at the center of the absorber and the center of the upper aerogel surface to correspond directly to the experimental thermocouple locations.

Fig. S8a shows the full 3D computational geometry constructed according to the finite size experimental configuration. Fig. S8b compares the experimentally measured

temperature histories with the full 3D predictions. The full 3D model reproduced both the transient heating process and the final stagnation temperatures well. The maximum absolute deviations were 8.2 °C for the absorber and 5.1 °C for the upper aerogel surface. At 7200 s, the corresponding deviations decreased to 3.1 °C and 0.8 °C, respectively.

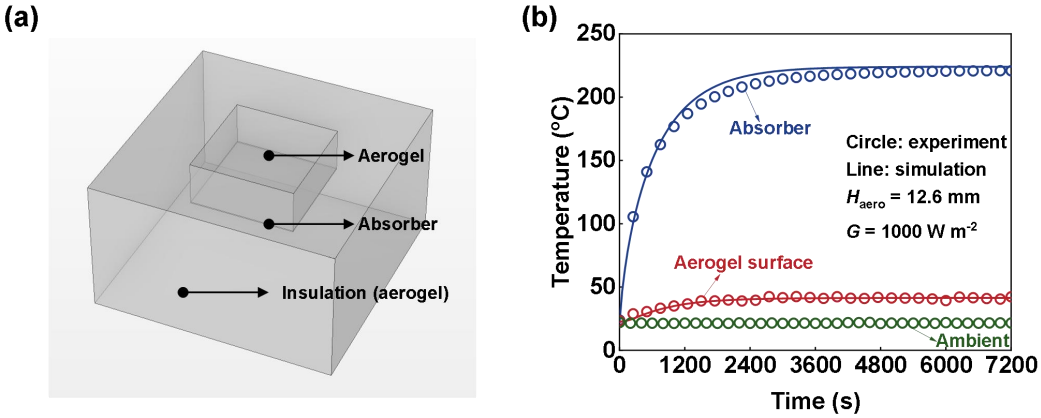


Figure S8. Full 3D model and experimental validation under stagnation conditions. (a) 3D computational geometry of the experimental configuration, including the aerogel, absorber, and surrounding insulation. (b) Comparison of the experimentally measured and full 3D predicted transient temperatures of the absorber and upper aerogel surface.

To assess the influence of dimensionality, the original 2D model was subsequently calculated using the same intrinsic material properties as the validated 3D model. As shown in Fig. S9, the uncorrected 2D model predicted a higher absorber temperature, with a maximum difference of 47.4 °C relative to the 3D result. The difference arises because the 2D formulation does not explicitly resolve out of plane heat spreading and the additional edge heat loss pathways associated with the finite lateral dimensions of the experimental receiver.

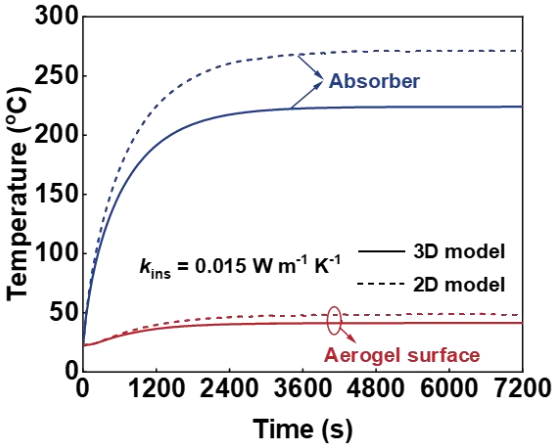


Figure S9. Comparison of the uncorrected 2D and full 3D transient temperature histories using the same intrinsic material properties, illustrating the finite size effect neglected in the 2D formulation.

Although the full 3D model provides a more complete representation of the finite size receiver, its computational cost is substantially higher. Under the same computational environment and comparable convergence settings, with COMSOL Multiphysics configured to use 128 CPU cores for each simulation, a typical transient calculation required 20 min for the 2D model and 38 h for the corresponding 3D model. Considering the large number of transient simulations required for the transport coupling, flow response, and GHI driven regulation analyses, a calibrated 2D reduced order model was therefore adopted for the subsequent calculations.

An effective insulation thermal conductivity (k_{eff}), was introduced as a closure parameter in the 2D model to represent the additional heat dissipation caused by the 3D finite size effects. The value of k_{eff} was calibrated against the validated 3D temperature response rather than directly against the experimental data. The resulting value was k_{eff} = 0.026 W m^{-1} K^{-1}, compared with the intrinsic insulation thermal conductivity of 0.015 W m^{-1} K^{-1}. As shown in Fig. S10, the calibrated 2D model reproduced the 3D temperature histories closely, with maximum differences of 2.8 °C for the absorber and 0.2 °C for the upper aerogel surface. The same k_{eff} was retained in all subsequent 2D calculations involving the insulation domain without further fitting.

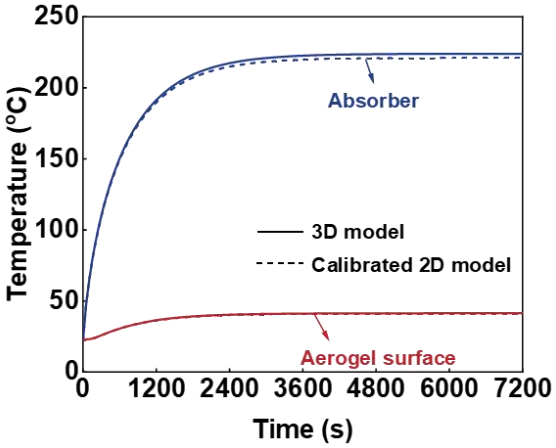


Figure S10. Comparison of the calibrated 2D and full 3D transient temperature histories after introducing the effective insulation thermal conductivity (k_{eff}), in the reduced order model.

The overall heat loss characteristics were further assessed by comparing the full 3D model with the calibrated 2D model. Fig. S11 shows the energy breakdown predicted by the full 3D model under the stagnation condition, while the corresponding calibrated 2D result is presented in Fig. 2e of the main text. For quantitative comparison, the heat losses through the side and bottom insulation boundaries were combined, and the convective and radiative losses from the upper aerogel surface were combined as the top surface heat loss. The combined side and bottom heat losses accounted for 57.9% and 57.5% of the incident solar energy in the calibrated 2D and full 3D models, respectively, corresponding to a difference of only 0.4 percentage points. The corresponding top surface heat loss fractions were 31.3% and 31.6%, with a difference of only 0.3 percentage points. The close agreement in both heat loss categories indicates that the calibrated 2D model preserves the principal energy loss characteristics of the full 3D receiver in addition to reproducing its transient temperature response.

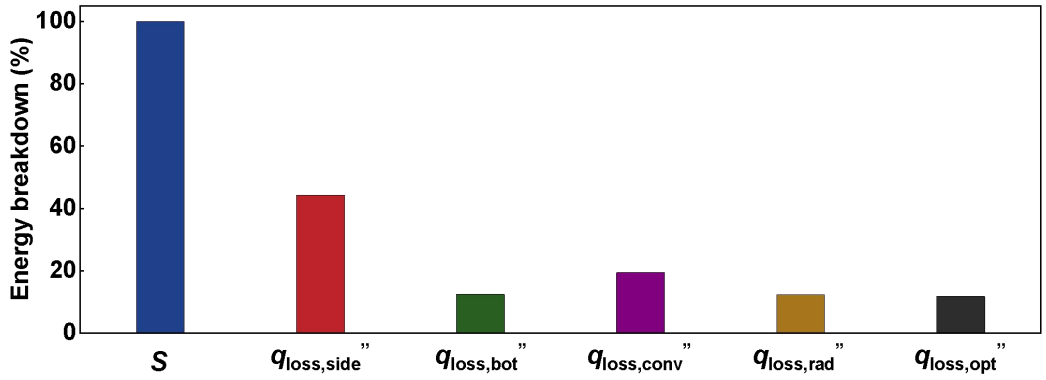


Figure S11. Energy breakdown predicted by the full 3D model under the stagnation condition, showing the relative contributions of the principal heat loss pathways.

S4.6 Sensitivity to short-wave solar absorption in the aerogel

The influence of direct short-wave solar absorption within the silica aerogel was evaluated through an additional sensitivity calculation. Previous spectral analysis showed that attenuation of transparent silica aerogels in the range of 1000–2500 nm is dominated by absorption. Accordingly, the spectral absorptance in this range was approximated as 1-T_λ using the measured total transmittance of the aerogel. Weighting this absorbed fraction by the AM 1.5G spectrum relative to the total incident solar energy over 250–2500 nm gave an estimated effective solar-weighted absorptance of 3%:

$$\alpha_{\text{aero,solar}}^{\text{eff}} = \frac{\int_{1000}^{2500} (1-T_\lambda) I_{\text{AM1.5G},\lambda} d\lambda}{\int_{250}^{2500} I_{\text{AM1.5G},\lambda} d\lambda} \tag{S24}$$

At an incident irradiance of 1000 W m^{-2}, the corresponding absorbed solar flux was 30 W m^{-2}. This energy was introduced into the 12.6 mm thick aerogel as an equivalent uniformly distributed volumetric heat source:

$$Q_{\text{sw}} = \frac{S\alpha_{\text{aero,solar}}^{\text{eff}}}{H_{\text{aero}}} \tag{S25}$$

Fig. S12 compares the transient absorber and upper aerogel surface temperatures

predicted with and without this additional short-wave solar absorption. The maximum temperature differences were 3.4 °C for the absorber and 1.3 °C for the upper aerogel surface, while the corresponding steady-state differences were 2.7 °C and 1.1 °C, respectively. The close agreement indicates that direct short-wave solar absorption within the aerogel has only a minor influence on the predicted thermal response. It was therefore neglected in the baseline model.

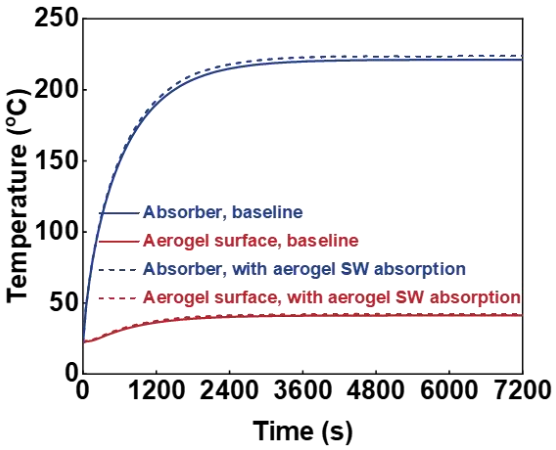


Figure S12. Sensitivity of the transient absorber and upper aerogel surface temperatures to short-wave solar absorption within the silica aerogel under an incident irradiance of 1000 W m^{-2}. Solid lines represent the baseline model, while dashed lines include an equivalent volumetric heat source of 2381 W m^{-3}, corresponding to an estimated effective solar-weighted aerogel absorptance of 3%.

Supporting Note S5. Heat flux evaluation

Heat fluxes were evaluated at the aerogel-absorber interface and the upper aerogel boundary (Fig. S13). At each location, the reported value was obtained by averaging the corresponding normal heat flux along the horizontal evaluation line. The same evaluation locations were used for the coupled, conduction only, and radiation only cases. A common positive direction was defined from the absorber toward the upper aerogel surface and was applied consistently to all heat flux comparisons.

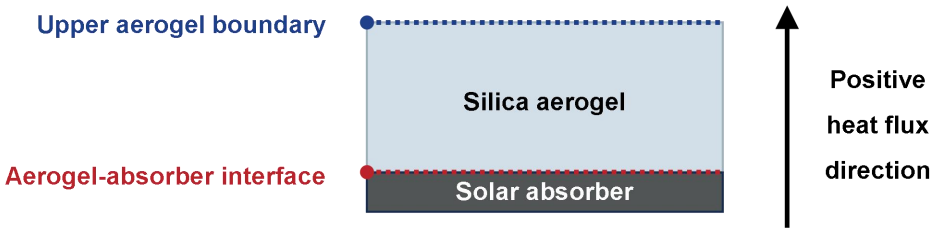


Figure S13. Heat flux evaluation locations and sign convention.

Supporting Note S6. Step response analysis

S6.1 Step response protocol

Step response simulations were performed using the fully coupled fluid flow model at fixed inlet velocities of 2×10^{-4}, 4×10^{-4}, 6×10^{-4}, 8×10^{-4}, 1×10^{-3}, and 1.2×10^{-3} m s^{-1}. The inlet temperature and initial temperature of all computational domains were maintained at 22 ^{o}C. Solar irradiance was set to 1000 W m^{-2} for the first 3600 s and was then reduced to 600 W m^{-2} for a further 3600 s. All other boundary conditions and numerical settings were kept unchanged among the 6 cases. The resulting outlet temperature histories were used to determine the heating and cooling response characteristics described in Section S6.2.

S6.2 Response time extraction and curve fitting

The outlet response time was determined directly from the simulated temperature history using the 63.2% criterion defined in the main text. For each inlet velocity, the heating and cooling stages were evaluated separately using their respective initial and final steady outlet temperatures. The response time was taken as the elapsed time from the irradiance change to the point at which the outlet temperature reached 63.2% of the corresponding total temperature change. This procedure was applied directly to the numerical response and did not require an assumed response function.

The outlet temperature histories were additionally fitted using a single exponential response to characterize the overall transient behavior. The fitted curves were used only to assess the response shape and were not used to determine the response times reported in the main text. The complete response metrics for the investigated inlet velocities are summarized in Section S6.3.

S6.3 Complete response metrics

The outlet temperature response metrics for the six inlet velocities are summarized in Tables S4 and S5. During heating at 1000 W m^{-2}, increasing the inlet velocity from 2×10^{-4} to 1.2×10^{-3} m s^{-1} reduced the steady outlet temperature from 127.3 to 45.0 ^{o}C and

shortened the response time from 523.6 to 91.9 s. After the irradiance decreased from 1000 to 600 W m^{-2}, the corresponding steady outlet temperature decreased from 85.9 to 35.8 °C, while the response time decreased from 526.7 to 91.6 s. The heating and cooling response times were similar at each inlet velocity. All fitted responses yielded coefficient of determination (R^2) values above 0.994, indicating good agreement between the fitted and simulated outlet temperature histories.

Table S4. Steady outlet temperatures, heating response times, and fitting quality at 1000 W m^{-2}.

Inlet velocity (m s^{-1})	$T_{out,ss}$ (°C)	τ_{out} (s)	R^2
2×10^{-4}	127.3	523.6	0.99992
4×10^{-4}	83.9	285.9	0.99951
6×10^{-4}	65.6	189.5	0.99857
8×10^{-4}	55.6	140.4	0.99740
1×10^{-3}	49.3	111.1	0.99616
1.2×10^{-3}	45.0	91.9	0.99499

Table S5. Steady outlet temperatures, cooling response times, and fitting quality following the irradiance decrease from 1000 to 600 W m^{-2}.

Inlet velocity (m s^{-1})	$T_{out,ss}$ (°C)	τ_{out} (s)	R^2
2×10^{-4}	85.9	526.7	0.99999
4×10^{-4}	59.3	286.8	0.99952
6×10^{-4}	48.2	189.9	0.99859
8×10^{-4}	42.2	141.0	0.99730
1×10^{-3}	38.4	110.7	0.99601
1.2×10^{-3}	35.8	91.6	0.99491

Supporting Note S7. Implementation of *GHI*-driven flow regulation

S7.1 The *GHI* measurements in Shenzhen

The *GHI* was measured in Shenzhen, China, and used as the time-dependent solar input for the flow-regulation simulations. 3 representative daytime *GHI* profiles were selected to cover distinct irradiance conditions, including a fluctuating condition with a brief low-irradiance interruption, an intermittent condition with an extended period close to the flow-on threshold, and a sunny condition with short cloud-induced fluctuations. The selected profiles correspond to 1 July, 9 July, and 11 July 2026, respectively.

The *GHI* was measured using a compact weather station equipped with a thermopile pyranometer (Shandong Renke Control Technology Co., Ltd., China), as shown in Fig. S14. The irradiance was recorded at a sampling interval of 60 s. The measured *GHI* time series was directly prescribed as the transient solar irradiance, $S(t)$, in the numerical simulations.



Figure S14. Compact weather station used for *GHI* measurements in Shenzhen.

The measured *GHI* profiles were used as transient solar inputs for the receiver system considered in the *GHI*-driven flow regulation simulations.

S7.2 Solar receiver system configuration

The schematic configuration of the solar receiver system considered in the GHI-driven flow regulation simulations is illustrated in Fig. S15. The system consists of a transparent aerogel-covered receiver, solar absorber, fluid channel, circulation loop, pump, flow meter, cooling reservoir, and inlet/outlet temperature measurement locations.

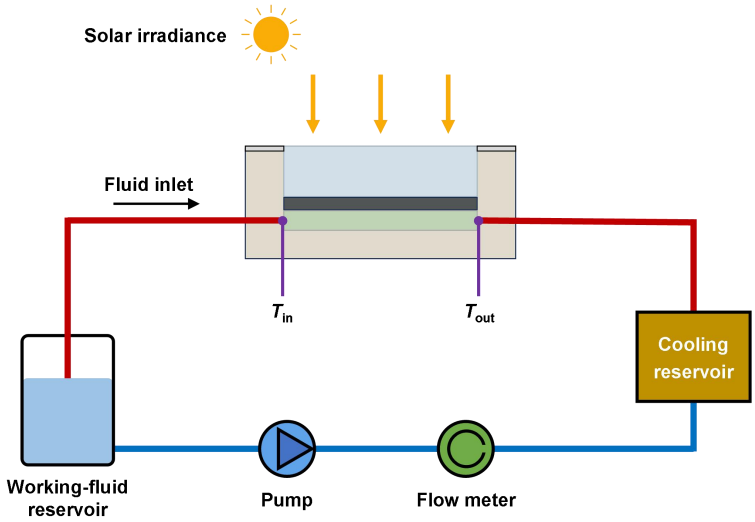


Figure S15. Schematic illustration of the solar receiver system configuration considered in the GHI-driven flow regulation simulations. The schematic includes the transparent aerogel-covered receiver, solar absorber, fluid channel, circulation loop, pump, flow meter, cooling reservoir, and temperature measurement locations.

S7.3 Operating map construction and interpolation

The steady operating map was constructed from the fully coupled fluid flow model by calculating the steady outlet temperature over discrete combinations of solar irradiance and inlet velocity within the investigated operating range. For each operating point, the simulation was continued until the thermal state became time independent, and the corresponding mass-flow-weighted outlet temperature was recorded. The discrete results were then interpolated to obtain a continuous relation between S, v_{in}, and $T_{out,ss}$.

For the prescribed outlet temperature target of 50 °C, the required inlet velocity was obtained from the 50 °C contours of the interpolated operating map. This contour defined the setpoint function $v_{set}(S)$ used in the transient regulation simulations. A setpoint was assigned only when the target temperature could be achieved within the investigated velocity range. When no feasible operating point existed, the flow was switched off according to the criterion defined in the main text.

S7.4 Inlet velocity schedules

The inlet velocity schedules used in the transient regulation simulations were generated by combining the measured *GHI* profiles with the setpoint relation $v_{set}(S)$ obtained in Section S7.3. At each adjustment time, the instantaneous measured GHI was mapped to the corresponding velocity setpoint. Successive setpoints were connected using the 5-s cubic ramp defined in the main text and were then maintained until the next adjustment. When the measured *GHI* fell outside the feasible operating range for maintaining the target outlet temperature, the inlet velocity was set to 0.

Fig. S16 shows the resulting inlet velocity histories for adjustment intervals of 60, 120, 180, 240, and 300 s under the 3 measured *GHI* conditions. Shorter adjustment intervals retain more of the temporal variation in the required flow rate, whereas longer intervals produce longer periods of constant inlet velocity between successive updates. The 0-velocity segments correspond to periods in which the measured *GHI* was below the flow-on threshold. These prescribed velocity histories were applied directly as the inlet boundary condition in the transient simulations, while the measured *GHI* time series remained the solar input $S(t)$.

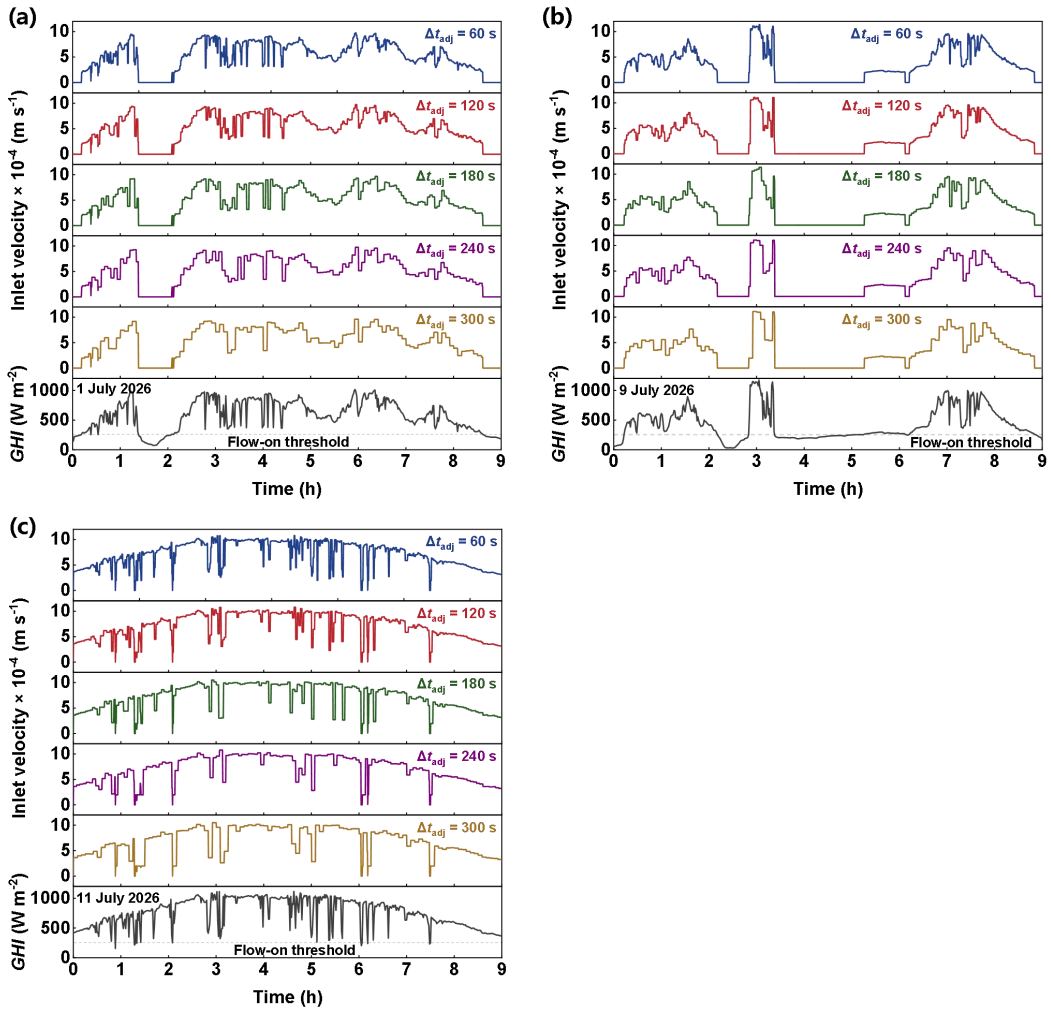


Figure S16. Inlet velocity schedules generated for the 3 measured *GHI* profiles at adjustment intervals of 60–300 s.

S7.5 Implementation workflow of *GHI*-driven flow regulation

The implementation procedure of the *GHI*-driven flow regulation strategy is summarized in Fig. S17. The measured *GHI* profile is introduced as the transient solar input. The required inlet velocity is determined from the precomputed steady operating map through inverse interpolation and subsequently applied to the transient receiver model to evaluate the regulated outlet temperature response.

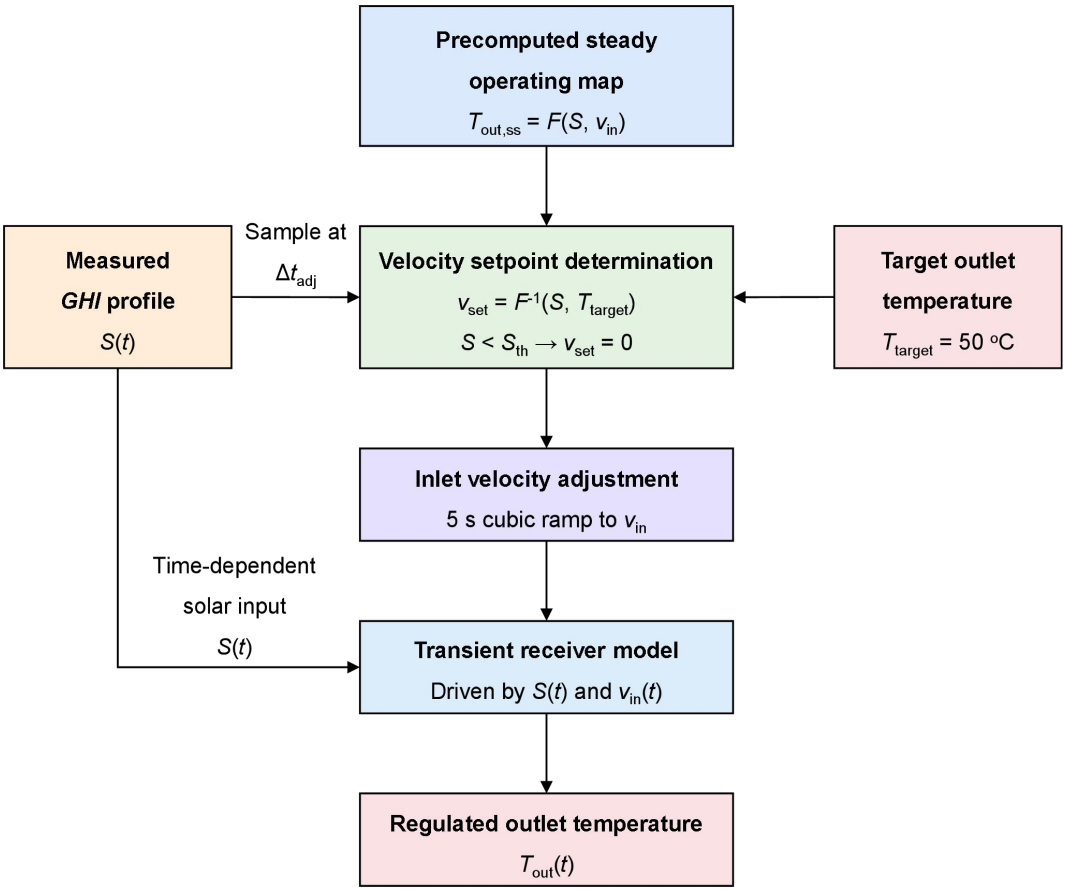


Figure S17. Workflow of the *GHI*-driven flow regulation strategy. The measured *GHI* profile is used as the transient solar input. The inlet velocity setpoint is determined from the precomputed steady operating map through inverse interpolation and subsequently applied to the transient receiver model to evaluate the regulated outlet temperature response.

References

(1) Li, S.; Liu, S.; Yang, Q.; Deng, S.; Lin, M. Cover Matters: Enhanced Performance of a Multistage Solar Evaporator with Tuned Optical and Thermal Cover Properties. *Energy Environ. Sci.* **2025**, *18* (1), 275–283. https://doi.org/10.1039/D4EE02710H

(2) Li, S.; Zhang, J.; Chen, Y.; Liu, S.; Lu, W.; Deng, S.; Lin, M. Tuning Radiative Properties of Multiscale Porous Transparent Silica Aerogels for Efficient Solar Interfacial Evaporation. *Adv Funct Materials* **2026**, *36* (27), e28287. https://doi.org/10.1002/adfm.202528287

(3) Qiu, Y.; Zhang, Y.; Li, Q.; Xu, Y.; Wen, Z.-X. A Novel Parabolic Trough Receiver Enhanced by Integrating a Transparent Aerogel and Wing-like Mirrors. *Applied Energy* **2020**, *279*, 115810. https://doi.org/10.1016/j.apenergy.2020.115810

(4) Li, X.; Li, R.; Chang, H.; Zeng, L.; Xi, Z.; Li, Y. Numerical Simulation of a Cavity Receiver Enhanced with Transparent Aerogel for Parabolic Dish Solar Power Generation. *Energy* **2022**, *246*, 123358. https://doi.org/10.1016/j.energy.2022.123358

(5) Ye, K.; Li, Q.; Zhang, Y.; Qiu, Y.; Liu, B. An Efficient Receiver Tube Enhanced by a Solar Transparent Aerogel for Solar Power Tower. *Energy* **2022**, *261*, 125313. https://doi.org/10.1016/j.energy.2022.125313

(6) Caps, R.; Fricke, J. Infrared Radiative Heat Transfer in Highly Transparent Silica Aerogel. *Solar Energy* **1986**, *36* (4), 361–364. https://doi.org/10.1016/0038-092X(86)90153-2

(7) Cohen, E.; Glicksman, L. Thermal Properties of Silica Aerogel Formula. *Journal of Heat Transfer* **2015**, *137* (8), 081601. https://doi.org/10.1115/1.4028901

(8) Günay, A. A.; Kim, H.; Nagarajan, N.; Lopez, M.; Kantharaj, R.; Alsaati, A.; Marconnet, A.; Lenert, A.; Miljkovic, N. Optically Transparent Thermally Insulating Silica Aerogels for Solar Thermal Insulation. *ACS Appl. Mater. Interfaces* **2018**, *10* (15), 12603–12611. https://doi.org/10.1021/acsami.7b18856

(9) Frisvad, J. R.; Christensen, N. J.; Jensen, H. W. Computing the Scattering Properties of Participating Media Using Lorenz-Mie Theory. *ACM Trans. Graph.* **2007**, *26* (3), 60. https://doi.org/10.1145/1276377.1276452

(10) Zhao, L.; Bhatia, B.; Yang, S.; Strobach, E.; Weinstein, L. A.; Cooper, T. A.; Chen, G.; Wang, E. N. Harnessing Heat Beyond 200 °C from Unconcentrated Sunlight with Nonevacuated Transparent Aerogels. *ACS Nano* **2019**, *13* (7), 7508–7516. https://doi.org/10.1021/acsnano.9b02976

(11) Liu, S.; Fan, F.; Wang, A.; Xu, W.; Zhao, L.; Chen, R. 3D Simulation and Performance Analysis of the Non-Isothermal Charge/Discharge Processes in Thermo-Electrochemical Cycle. *Journal of Power Sources* **2026**, *661*, 238695. https://doi.org/10.1016/j.jpowsour.2025.238695